

# Inclusion of Inter-crystal Scattering in PET: Analytical Models and Dedicated Reconstruction

Jorge Roser, *Member, IEEE*, Hong Phuc Vo, *Graduate Student Member, IEEE*, Rebecca Kantorek, Steven Seeger, *Member, IEEE*, and Magdalena Rafecas, *Senior Member, IEEE*

**Abstract**—Inter-crystal scattering (ICS) in Positron Emission Tomography (PET) is commonly regarded as a degradation effect that might compromise the image spatial resolution. In parallel, the inclusion of ICS events has also been recognized as a potential approach to increase PET sensitivity, which could be especially beneficial in scenarios where the latter is a limiting factor, such as very small animal imaging. Several methods for the recovery of ICS events have been proposed, many of which aim to locate the first interaction, i.e., the Compton scattering site, usually limited by their success rate, computational burden or data and training dependency. Conversely, this work proposes a physics-based model for ICS events, leading to analytical expressions of the sensitivity image and the system matrix (required by statistical reconstruction algorithms), without the need to identify the original line of response. After validating the model, the work shows how ICS events can be integrated into a joint image reconstruction algorithm (based on list-mode MLEM) together with conventional PET events, for which dedicated analytical models are also developed. To assess the performance of the proposed approach, Monte-Carlo simulated and experimental data of an image quality phantom were obtained with the MERMAID small-fish PET scanner prototype. Both simulation and experimental results indicate that, while slightly decreasing the recovery coefficient values, the inclusion of ICS clearly reduces statistical noise and improves uniformity.

**Index Terms**—Inter-crystal scattering, detector scatter, ICS, PET, image reconstruction, sensitivity

## I. INTRODUCTION

THE quest for increased sensitivity has motivated advances in Positron Emission Tomography (PET) since the very beginning of this nuclear imaging technique. Improving the sensitivity of PET systems is essential to allow for dose and/or scan time reduction [1]; in addition, sensitivity can be a limiting factor in low-count PET scenarios. These scenarios include imaging certain segments of the population (e.g. pediatric [2] or pregnant [3]), dynamic PET, PET-based  $^{90}\text{Y}$  dosimetry [4], as well as some specific applications like range verification in particle therapy [5] by means of PET, and preclinical PET with very small animals such as zebrafish [6], where the amount of radiotracer that can be administered to research animals is very small.

To increase the sensitivity of PET scanners, several approaches have been proposed, some of them already implemented in commercial systems, like the extension of the

axial field of view (total-body PET [7]), the use of organ-specific designs [8], [9] and larger scintillation crystals [10] or the application of wider energy windows [11]. A different, albeit complementary approach is the inclusion of inter-crystal scattering (ICS) events. In an ICS event, at least one of the annihilation photons undergoes Compton scattering in a given PET detector, prior to the absorption of the scattered photon in a different detector. It follows that an ICS event is characterized by at least three hits in different PET detectors, as opposed to those conventional events in which both annihilation photons are directly absorbed, yielding two hits and hereafter referred to as *golden* events. The term *hit* refers here to the physical photon interaction, regardless of whether it is eventually detected or not<sup>1</sup>; furthermore, *PET detector* refers here to the smallest detection unit capable of discriminating hits. Therefore, the concept of ICS also excludes that of *intracrystal scattering*, in which the Compton scattering and the eventual absorption of the scattered photon happen in the same PET detector.

In the last years, ICS in PET has received renewed attention, as some modern high-resolution detector designs - with two or more layers of small, tightly packed crystals - promote Compton scattering of the photons [12], [13]. Indeed, if properly handled, the detected ICS events fraction can significantly contribute to increase the system efficiency [14]. A common problem encountered with such events is the need to identify the Compton scattering site. For this reason, most of the ICS-recovery strategies focus on determining the position of the Compton scattering in order to obtain the correct line of response (LOR) [15], either exploiting the energy information [16], Compton kinematics [14], [17], optimization algorithms [18], [19] or neural networks [20], [21], [22], [12]. These strategies, however, entail the risk of incorrectly estimating the primary photon trajectory, thus introducing a number of *wrong* LORs into the reconstruction, i.e., events carrying incorrect information about the spatial emission distribution. Such wrong LORs can compromise the attainable image quality and alter the activity quantification, especially for ICS-recovery methods with low accuracy. Even though some of the aforementioned event-selection strategies have reported notably high ICS identification accuracy (e.g. 98 % [19]), they require either significant computational resources, prior

This work did not involve human subjects or animals in its research.

J. Roser, H. P. Vo, R. Kantorek and M. Rafecas are with the Institute of Medical Engineering, Universität zu Lübeck, Germany (e-mail: jorge.rosermartinez@uni-luebeck.de).

R. Kantorek and S. Seeger are with the Isotope Laboratory of the Natural Science Section, Universität zu Lübeck, Germany.

<sup>1</sup>For instance, depending on the energy window, some Compton scattering interactions might remain undetected with the subsequent second interaction being assigned to the coincidence event, thus *disguising* an ICS event as a golden one; this effect becomes more pronounced the worse the energy resolution.

information, a particular PET geometry, or extensive data and training [15].

Conversely, an alternative approach is to model the system response to ICS events, which leads naturally to V-shaped LORs [23]. Response models are a key element of statistical iterative reconstruction, such as List-Mode Maximum-Likelihood Expectation-Maximization (LM-MLEM), through the so-called *system matrix*  $\mathbf{H}$  and *sensitivity image*  $\mathbf{s}$ :

$$\boldsymbol{\lambda}^{(n+1)} = \boldsymbol{\lambda}^{(n)} \oslash \mathbf{s} \odot \left( \mathbf{H}^\top \left( \mathbf{1} \oslash (\mathbf{H} \boldsymbol{\lambda}^{(n)}) \right) \right) \quad (1)$$

where  $\boldsymbol{\lambda}^{(n)}$  is the image vector after the  $n$ -th iteration,  $\mathbf{1}$  is a column vector of ones of length equal to the number of detected events;  $\odot$  and  $\oslash$  represent element-wise multiplication and element-wise division, respectively. An element of the system matrix,  $h_{iv}$ , represents the probability that an emission from image element  $v$  (usually a voxel) is detected as the measurement element  $i$ ; whereas an element of the sensitivity image,  $s_v$ , denotes the overall detection probability of an emission from  $v$ . The ability of the models behind  $\mathbf{H}$  and  $\mathbf{s}$  to capture the underlying physics significantly determines the image quality.

Measurement elements encoded by V-LORs are less informative than regular LORs, or equivalently, the rows of the corresponding ICS system matrix  $\mathbf{H}^I$  have higher intricacy<sup>2</sup> than those of the golden system matrix  $\mathbf{H}^G$ ; nonetheless, V-LORs carry useful information about the spatial emission distribution. In this way, golden and ICS events can be treated as two separated channels of information from which independent, accurate estimations of the object spatial emission distribution can be obtained; for instance, by applying (1) separately to golden events modeled as LORs through  $\mathbf{H}^G$ , and  $\mathbf{s}^G$ , and to ICS events modeled as V-LORs through  $\mathbf{H}^I$ , and  $\mathbf{s}^I$ . However, and importantly, both channels *together* can provide an estimate of the activity distribution via a joint image reconstruction algorithm [23], [24], [25], the resulting image quality being potentially superior to that obtained using only golden or ICS events, especially in the low-count regime.

The present work explores and extends this approach by developing a dedicated analytical model for ICS events based on the physics behind the photon emission and detector interactions, which is integrated into the LM-MLEM algorithm (although it is not restricted to it) and implemented for a very small-animal PET scanner. The study shows how the new model provides reasonably accurate estimations of the ICS sensitivity image  $\mathbf{s}^I$  and the system matrix  $\mathbf{H}^I$ . As the concept of V-LORs takes into account the two possible trajectories, while only one is the original one, some degradation of the spatial resolution and other metrics could be expected. Therefore, this study also assesses the image quality obtained with the inclusion of ICS events modeled in this way, compared to reconstructing only golden events. In particular, the developed model targets three-hit ICS events, i.e., those featuring a single Compton scattering, as such events are typically far more frequent than four-or-more hit ICS events. For a fair comparison and also to correctly implement the joint

<sup>2</sup>Another interpretation would be that the ICS system matrix  $\mathbf{H}^I$  is less sparse than the golden one,  $\mathbf{H}^G$ .

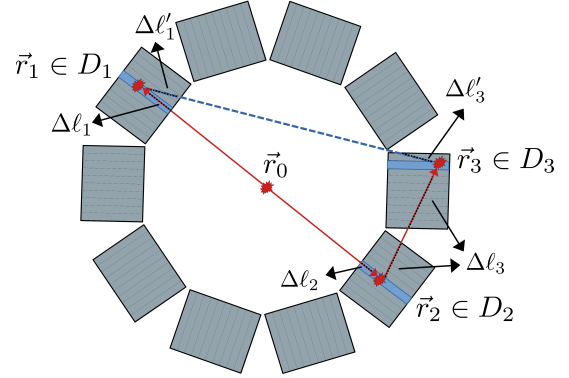


Fig. 1. Scheme of an ICS event with relevant quantities of the proposed analytical model. The red lines indicate the photon trajectories. The PET detector elements where the physical interactions occur are highlighted in light blue. In particular, the Compton scattering takes place in  $\vec{r}_2$ .

reconstruction approach, this work also introduces a dedicated analytical model for the golden events, also guided by a probabilistic formulation of physical phenomena analogous to that of the ICS model. The methods are applied to both simulated and experimental data, with a focus on very low-count acquisitions.

The remainder of the work is structured as follows. In section II, the analytical model for ICS events is formulated, mathematical expressions for the sensitivity image and the system matrix are derived, and the conducted experiments and Monte Carlo simulations are described. Section III shows the obtained results, which are subsequently discussed in section IV. Finally, section V summarizes the conclusions. In addition, three appendices have been included: Appendix A describes the employed nomenclature, Appendix B provides details of the analytical model used for golden events, and Appendix C expands some of the results.

## II. METHODS AND MATERIALS

Firstly, the analytical model leading to the mathematical expressions for the ICS sensitivity image  $\mathbf{s}^I$  and system matrix  $\mathbf{H}^I$  is presented, followed by their integration into a dedicated joint image reconstruction formalism. The nomenclature employed can be found in table III (Appendix A). Finally, the conducted experiments and Monte Carlo simulations are described.

### A. Analytical model for ICS events

Similar to [26], the expressions for the system matrix and the sensitivity image are derived from the differential probability of an emission to become a true event in the detector. In this work, an emission refers to a positron-electron annihilation yielding two photons, and the true event is a three-hit ICS in which one annihilation photon is photoabsorbed in detector  $D_1$  whereas the other annihilation photon undergoes a Compton scatter in detector  $D_2$  and is photoabsorbed in detector  $D_3$ ; a scheme of such event is provided in figure 1.

The corresponding differential probability, denoted as  $dP_{123}^I$ , can be formulated as

$$dP_{123}^I = 2 \cdot dP(\vec{r}_0|v) dP(\Omega_0\Omega'_0|v\vec{r}_0\Omega_0 = -\Omega'_0) dP(\ell_1|v\vec{r}_0\Omega'_0) \cdot dP(\ell_2 d\Omega_2 d\ell_3|v\vec{r}_0\Omega_0). \quad (2)$$

In (2), the leading factor 2 accounts for the fact that one annihilation photon undergoes direct photoabsorption whereas the other photon does not, and it is irrelevant which one undergoes which of the interactions. The term

$$dP(\vec{r}_0|v) = \frac{d^3 r_0}{V} \Theta_v(\vec{r}_0) \quad (3)$$

corresponds to the differential probability of both annihilation photons to be emitted at position  $\vec{r}_0$  inside image element  $v$  (with volume  $V$ ), whose limits are given by the indicator function  $\Theta_v$ . Furthermore,

$$dP(\Omega_0\Omega'_0|v\vec{r}_0\Omega_0 = -\Omega'_0) = \frac{d\Omega_0}{4\pi} \frac{d\Omega'_0}{4\pi} 4\pi \delta(\Omega_0 + \Omega'_0) \quad (4)$$

corresponds to the differential probability for one annihilation photon to be emitted in a direction and the other in the exact opposite direction, being  $\Omega_0$  and  $\Omega'_0$  the solid angles representing the two directions, respectively. In other words, acolinearity is not considered in the model.

Next, the differential probability of one annihilation photon to survive a distance  $\Delta\ell_1$  in any detector material prior to photoelectric absorption in  $D_1$  is accounted for by

$$dP(\ell_1|v\vec{r}_0\Omega_0) = e^{-\mu_0\Delta\ell_1} \mu_0^e d\ell_1, \quad (5)$$

whereas the ICS part is represented by

$$dP(\ell_2 d\Omega_2 d\ell_3|v\vec{r}_0\Omega'_0) = e^{-\mu_0\Delta\ell_2} n_e \frac{d\sigma_0^C}{d\Omega_2} d\Omega_2 d\ell_2 e^{-\mu_2\Delta\ell_3} \mu_2 d\ell_3, \quad (6)$$

with  $\Delta\ell_2$  being the distance over which the annihilation photon survives in any detector material before undergoing Compton scattering in  $D_2$ , and  $\Delta\ell_3$  being the distance over which the Compton-scattered photon survives in any detector material before undergoing photoelectric effect in  $D_3$ . For the sake of simplicity, this formulation of the model assumes a single-material PET surrounded by vacuum; however, further materials could be included by replacing the exponents in (5) and (6) by the corresponding sum over the involved distances and attenuation coefficients.

By integrating  $dP_{123}^I$  over the entire voxel volume  $V$ , all possible emission and Compton scattering directions, and all possible lengths  $\ell_1, \ell_2, \ell_3$  over the whole PET extent, an expression for the probability of an annihilation originated in voxel  $v$  to be detected anywhere in the PET scanner as an ICS event is obtained. This is precisely the definition of the ICS sensitivity image element,

$$s_v^I = \frac{2}{4\pi V} \int_{\vec{r}_0 \in v} d^3 r_0 \int_{\Omega_0 \in S^2} d\Omega_0 \int_{\vec{r}_0 - \ell_1 \hat{\Omega}_0 \in \text{PET}} d\ell_1 e^{-\mu_0\Delta\ell_1} \mu_0^e \cdot \int_{\substack{\vec{r}_0 + \ell_2 \hat{\Omega}_2 \in \text{PET} \\ \vec{r}_2 + \ell_3 \hat{\Omega}_2 \in \text{PET} \\ \Omega_2 \in S^2}} d\ell_2 d\ell_3 d\Omega_2 e^{-\mu_0\Delta\ell_2} n_e \frac{d\sigma_0^C}{d\Omega_2} e^{-\mu_2\Delta\ell_3} \mu_2^e, \quad (7)$$

which can be readily computed e.g. via Monte Carlo numerical integration methods.

Now, the change of variables  $\{\vec{r}_0, \Omega_0, \ell_1, \ell_2, \Omega_2, \ell_3\} \rightarrow \{\vec{r}_1, \vec{r}_2, \vec{r}_3, \xi\}$  allows  $dP_{123}^I$  to be expressed as

$$dP_{123}^I = \frac{2}{4\pi V} d^3 r_1 d^3 r_2 d\xi \Theta_v(\xi) \frac{e^{-\mu_0(\Delta\ell_1 + \Delta\ell_2)} \mu_0^e}{|\vec{r}_1 - \vec{r}_2|^2} d^3 r_3 \cdot n_e \frac{d\sigma_0^C}{d\Omega_2} \frac{e^{-\mu_2(\Delta\ell_3)} \mu_2^e}{|\vec{r}_3 - \vec{r}_2|^2}, \quad (8)$$

which, upon integration over the whole detector extent, leads to the following alternative expression for the sensitivity image:

$$s_v^I = \frac{2}{4\pi V} \int_{\vec{r}_1 \in \text{PET}} d^3 r_1 \int_{\vec{r}_2 \in \text{PET}} d^3 r_2 \int_{\xi \in \mathbb{R}^+} d\xi \Theta_v(\xi) \cdot \frac{e^{-\mu_0(\Delta\ell_1 + \Delta\ell_2)} \mu_0^e}{|\vec{r}_1 - \vec{r}_2|^2} \int_{\vec{r}_3 \in \text{PET}} d^3 r_3 n_e \frac{d\sigma_0^C}{d\Omega_2} \frac{e^{-\mu_2(\Delta\ell_3)} \mu_2^e}{|\vec{r}_3 - \vec{r}_2|^2}. \quad (9)$$

Equation (9) is particularly well-suited for numerical computation via ray-tracing methods [27]. Furthermore, the aforementioned change of variables allows obtaining the probability density:

$$\frac{dP_{123}^I}{d^3 r_1 d^3 r_2 d^3 r_3} = \frac{2}{4\pi V} \int_{\xi \in \mathbb{R}^+} d\xi \frac{e^{-\mu_0(\Delta\ell_1 + \Delta\ell_2)} \mu_0^e}{|\vec{r}_2 - \vec{r}_1|^2 |\vec{r}_3 - \vec{r}_2|^2} \Theta_v(\xi) n_e \frac{d\sigma_0^C}{d\Omega_2} e^{-\mu_2\Delta\ell_3} \mu_2^e. \quad (10)$$

An element of the ICS system matrix is defined as the probability of an annihilation originated in voxel  $v$  to be detected as an ICS event in the detector bin  $\Delta\eta_i = \{\Delta\vec{r}_1, \Delta\vec{r}_2, \Delta\vec{r}_3\}$ . In absence of further knowledge over the true Compton scattering site, the system matrix must be recognized as the sum of two terms, each one related to a possible detection sequence:  $dP_{123}^I$ , and  $dP_{132}^I$ , where the latter describes the differential probability of an ICS events in which the Compton scattering occurs in detector  $D_3$  and the scattered photon is absorbed in  $D_2$ . This second probability density is expressed as

$$\frac{dP_{132}^I}{d^3 r_1 d^3 r_2 d^3 r_3} = \frac{2}{4\pi V} \int_{\xi \in \mathbb{R}^+} d\xi \frac{e^{-\mu_0(\Delta\ell'_1 + \Delta\ell'_3)} \mu_0^e}{|\vec{r}_3 - \vec{r}_1|^2 |\vec{r}_3 - \vec{r}_2|^2} \Theta_v(\xi) n_e \frac{d\sigma_0^C}{d\Omega_3} e^{-\mu_3\Delta\ell_3} \mu_3^e. \quad (11)$$

Finally, an element of the system matrix can be formulated as

$$h_{iv}^I = w_1 \int_{\vec{r}_1, \vec{r}_2, \vec{r}_3 \in \Delta\eta_i} d^3 r_1 d^3 r_2 d^3 r_3 \frac{dP_{123}^I}{d^3 r_1 d^3 r_2 d^3 r_3} + w_2 \int_{\vec{r}_1, \vec{r}_2, \vec{r}_3 \in \Delta\eta_i} d^3 r_1 d^3 r_2 d^3 r_3 \frac{dP_{132}^I}{d^3 r_1 d^3 r_2 d^3 r_3} \quad (12)$$

which leads to V-shaped LORs with different weights arising from the physical factors in (10) and (11). The weights  $w_1$

and  $w_2$  allow conveying any additional knowledge over the Compton scattering site; if no such additional knowledge exists, then  $w_1 = w_2 = 1/2$ . The integration over the interaction positions is to be performed over the detector bin  $\Delta\eta_i = \{\Delta\vec{r}_1, \Delta\vec{r}_2, \Delta\vec{r}_3\}$  which, in the absence of further discretization, given e.g. by depth-of-interaction information, might be equal to the whole extent of the involved PET detectors, i.e.  $\Delta\eta_i = \{V_{D_1}, V_{D_2}, V_{D_3}\}$ . In this case, and under the assumption that (10) and (11) are slowly varying functions in the integration limits, the system matrix element can be approximated as:

$$h_{iv}^I \approx V_{D_1} V_{D_2} V_{D_3} \left( w_1 \frac{dP_{123}^I}{d^3r_1 d^3r_2 d^3r_3} + w_2 \frac{dP_{132}^I}{d^3r_1 d^3r_2 d^3r_3} \right). \quad (13)$$

Remarkably, the expressions derived here are not constrained to any particular PET geometry.

It must be noted that the estimation of the ICS sensitivity image expressions (7) and (9) involves the computation of angles, length or interaction positions that allow determining the Compton-scattered photon energy,  $E_2$ , by using the corresponding Compton equation [28]. This, in turn, allows implementing strategies to account for possible energy cuts applied over the ICS events. For instance, if (9) is estimated via Monte Carlo integration, each sampled point  $\{\vec{r}_1, \vec{r}_2, \vec{r}_3, \xi\}_n$  yields an energy  $E_{2,n}$ , which determines the deposited energy in  $D_2$  (equal to 511 keV -  $E_{2,n}$ ) and in  $D_3$  (equal to  $E_{2,n}$ ); if any of these deposited energies lies outside of the applied energy window used to acquire the ICS data, the contribution of the sampled point to the estimated integral is zero.

### B. Image reconstruction

The LM-MLEM algorithm was implemented as in (1) to obtain images with only ICS events (using the analytical sensitivity image (9) and system matrix (13) with equal weights  $w_1 = w_2 = 1/2$ ), and only golden events. For the latter, a dedicated model was also developed (see analytical expressions for the system matrix  $\mathbf{H}^G$  and sensitivity image  $\mathbf{s}^G$  in Appendix B). Furthermore, and similar to [23], [24], [25], the LM-MLEM was extended to allow for the joint reconstruction of ICS and golden events. The corresponding update equation is:

$$\lambda_v^{(n+1)} = \frac{\lambda_v^{(n)}}{s_v^G + s_v^I} \left( \sum_{i \in G} \frac{h_{iv}^G}{\sum_w h_{iw}^G \lambda_w^{(n)}} + \sum_{i \in I} \frac{h_{iv}^I}{\sum_w h_{iw}^I \lambda_w^{(n)}} \right), \quad (14)$$

where  $\lambda_v^{(n)}$  refers to the image value at the image element  $v$  and iteration  $n$ . Images were discretized using a grid of  $150 \times 150 \times 180$  cubic voxels with side length 0.25 mm, except when specified otherwise. Images obtained at different iteration numbers were analyzed, and no post-reconstruction smoothing was applied. No corrections (attenuation, object-scattering, normalization) were included into the reconstruction algorithm.

### C. Experimental setup

The derived analytical models were tested on MERMAID data. MERMAID stands for *Multi-Emission Radioisotopes - Marine Animal Imaging Device*, a small aquatic animal PET scanner prototype being developed at the Universität zu Lübeck [29]. The current prototype consists of four modules mounted on a rotating gantry, with a linear stage allowing for bed (axial) motion. Each module contains  $128 \times 64$  pixelated LYSO crystals ( $1.12 \times 1.12 \times 15$  mm $^3$  each) coupled one-to-one to Silicon Photomultipliers (Hamamatsu S13615-1050N-08) and readout by the PETsys Electronics TOFPET 2C ASIC. The energy resolution at 511 keV is 21.6 %. The readout allows retrieving the list of fired SiPM channels ordered by time. Coincidences were subsequently obtained offline by applying a temporal coincidence window of 2 ns and classified according to the number of fired SiPM channels and the energy deposited. Coincidences involving two SiPM channels depositing energy within [450, 550] were classified as golden, whereas coincidences involving three SiPM channels, with one energy deposition within [450, 550] keV and the other two within [180, 380] keV and [180, 550] keV, were classified as ICS events. The lower threshold of 180 keV was chosen as the lowest energy value that all the SiPM channels of the current prototype can reliably measure without being compromised by electronic noise and was taken into account in the corresponding ICS sensitivity image model. The upper threshold of 380 keV encompasses the maximum energy that a 511 keV photon can deposit in a Compton scattering (approximately 341 keV), with a margin to account for the energy resolution of the scanner. The remaining coincidences were discarded. Compensation for radioactive decay was considered in the acquisition time per rotation and axial step.

The performance of the proposed models was assessed by means of an image quality (IQ) phantom adapted to the very-small-animal scenario. To this end, the design of the NU4-2008 (NU4) IQ phantom proposed by the National Electrical Manufacturers Association (NEMA) [30] was downsampled to the 50 % of its size; i.e. including a rods region with rod diameters of 2.50, 2.00, 1.50, 1.00 and 0.50 mm and equal height of 10 mm, a uniform region of diameter 15.0 mm and height of 15.0 mm, and an insert region with the same dimensions as the uniform region and with two inner, air-filled rods with diameter 4.0 mm. This downsampled IQ phantom was 3D-printed with  $^{18}\text{F}$ -FDG-labeled resin [31] with a total activity at the time of measurement of 0.27 MBq. This very low amount aims to mirror the challenging conditions that may arise in small-fish PET imaging. The full scan involved three rotation steps ( $60^\circ$  each) at ten different bed/axial positions separated 3 mm each; the total measurement time was approximately 50 minutes. The selected phantom activity and measurement parameters resulted in a low-count PET scenario, where image noise clearly strongly degraded the images (when compared to higher-activity phantom measurements conducted in preliminary experiments).

The reconstructed images of the rod and uniform regions of the IQ phantom were used to obtain the recovery coefficients (RCs) and the uniformity percentage standard devi-

ation (% STD), respectively. For this purpose, the protocols described in [30] were adapted to the downscaled size of the phantom. Note that the metrics were aimed to compare the proposed approach with the conventional reconstruction of golden events, and not for comparison with other PET systems. To compute the uniformity metric, a cylindrical Region-Of-Interest (ROI) centered in the uniform region of the phantom was defined with diameter 11.25 mm and height 5.00 mm. For the estimation of the RCs, the NEMA protocol was further modified in order to compensate for the degrading effects of the low counts. Specifically, cylindrical ROIs were defined for each rod with shared height of 5 mm and 75 % of their physical radii. Subsequently, the ROI was projected over the axial axis (Z-axis in this work), its mean being used for the RC computation. This procedure departs from the NEMA protocol, where the axial profiles at the maximum value of the averaged transversal ROI slices are used. As pointed out elsewhere [32], such a protocol might be sub-optimal as it overestimates systematically the RCs, especially in high-variance cases such as the ones expected in a low-count PET scenario. By contrast, the procedure employed in this work, also suggested in [32], was found to alleviate the overestimation of the RC values. Additionally, the inserts region of the IQ phantom was used to compute the Spill-Over-Ratio (SOR), again adapting the NEMA protocol to the downscaled size of the phantom. These results with the SOR metric, which is mainly indicative of the accuracy of attenuation of scatter corrections (not implemented in this work), can be found in Appendix C.

#### D. Monte-Carlo simulations

Simulations were conducted in GATE version 9.2 [33] reproducing MERMAID's geometry. Several back-to-back 511 keV photon sources were simulated, with different purposes.

*One-voxel sources:* Seven one-voxel sources (i.e. cubic-shaped, with 0.25 mm length size) were independently simulated at different positions of the X-axis (centered at  $\pm 15.125, \pm 10.125, \pm 5.125$  and  $0.125$  mm), with source activity of 1 MBq. Five realizations were acquired at each position, each realization comprising three rotation steps (1 s and  $60^\circ$  each) in a single axial step. These simulations were used to validate the analytical sensitivity image expression (9), by comparing the predictions of the model to the number of ICS events detected in the simulations at the voxels where the source was placed.

*Cylinder source:* A cylinder with diameter 8 mm and length 4 mm was simulated at the center of the Field of View (FOV), with uniform activity of 1 MBq. The simulation comprised three rotation steps (10 s and  $60^\circ$  each) in a single axial step. As such, the axial extent of the images was reduced in this case to 50 voxels. The acquired ICS and golden events, obtained using the energy windows applied experimentally, were reconstructed in order to assess the quantitative accuracy of the obtained images, thus indirectly supporting the validation of the models.

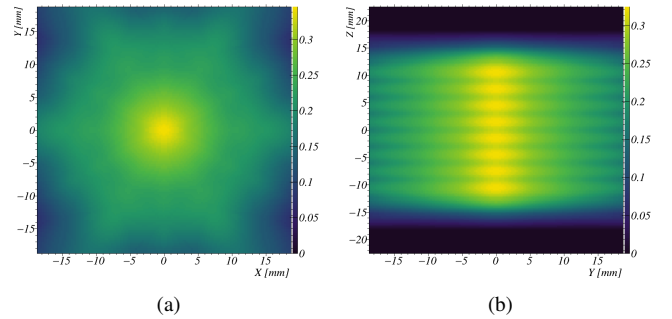


Fig. 2. Transversal (XY) and sagittal (YZ) projections over the analytical ICS sensitivity image, computed for the MERMAID geometry with 3 rotation steps and 10 bed positions, using (9) and assuming an energy threshold of 180 keV over the ICS events. The scale represent the probability of an annihilation emitted in a given group of voxels (e.g. a Z-row of voxels for the transversal projection) to be detected as an ICS event in MERMAID.

*IQ phantom:* The aforementioned IQ phantom was simulated, reproducing its downscaled size and activity. GATE's material database *Plastic* was chosen as phantom material. The purpose of this simulation was not to validate the experiments, but to assess the best attainable improvement in the images under close-to-ideal conditions. As such, MERMAID's detector spatial resolution was reproduced (limited to the pixelated crystal size) as well as the energy windows applied experimentally, but no further degradation effects (e.g. energy resolution or optical crosstalk) were modeled<sup>3</sup>.

In all simulation scenarios, the physics list `emstandard_opt3` was employed, together with production cuts of 1 mm.

#### E. Numerical estimation of the analytical expressions

The analytical expression for the ICS sensitivity image (9) was estimated via numerical Monte-Carlo (MC) integration. Sample points not fulfilling the event selection criteria described above (e.g. events outside the employed energy windows) did not contribute to the estimated integrals.

The attenuation coefficients in the models were obtained by using linear interpolation over the XCOM photon cross section database of the National Institute of Standards and Technology (NIST) [34], assuming the same LYSO composition and density ( $7.36 \text{ g} \cdot \text{cm}^{-3}$ ) as defined in the materials database of GATE version 9.2.

### III. RESULTS

#### A. ICS sensitivity image and system matrix

As a representative example of the outcome of (9), figures 2a and 2b show the transversal (XY) and sagittal (YZ) projections over the analytical ICS sensitivity image, for three rotation steps ( $60^\circ$ ), ten bed/axial positions with axial shift of 3 mm (i.e., with overlapping), and energy threshold of 180 keV over the ICS events. In particular, this ICS sensitivity image

<sup>3</sup>Time-related degradation effects (pile-up, temporal resolution, randoms) were equally not considered, although they are not expected to be relevant in this work given the low source activities involved.

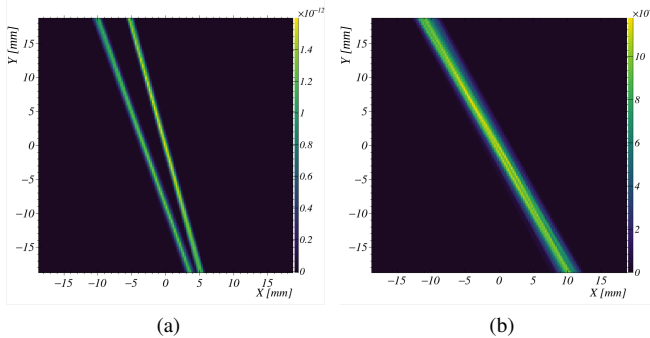


Fig. 3. Transversal ( $XY$ ) projections over two different analytical ICS system matrix rows, computed for the MERMAID geometry using (13). The scale represents the probability of annihilation emitted in a  $Z$ -row of voxels to be detected in terms of the particular measurement element considered.

was subsequently used to obtain images of the downscaled IQ phantom, both with experimental and MC-simulated data.

Likewise, figure 3 shows two examples of the estimation of ICS system matrix rows via (13); particularly, figure 3a illustrates the V-shape with which ICS events are modeled with the proposed approach. Such V-shape is not always conspicuous, especially when the interaction positions  $\vec{r}_2$  and  $\vec{r}_3$  occurs in closer-neighboring crystals, which is the case illustrated by figure 3b.

#### B. Validation of the analytical model

Table I lists the results of the validation of the analytical sensitivity image (9) with and without a threshold in 180 keV as well as including ICS events occurring in neighboring crystals, whereas table II lists the corresponding results excluding such neighboring-crystal ICS events. In all cases, the model predictions at seven different positions of the central  $X$ -axis are compared with the number of detected ICS events per back-to-back emission in the simulation. The five realizations simulated at each  $X$ -position allowed for an estimation of the mean and its standard error; as for the model, the Monte Carlo integration error was estimated.

TABLE I

ICS SENSITIVITY IMAGE VALUES AT SEVEN DIFFERENT POSITIONS OVER THE CENTRAL X-AXIS, FOR THE SIMULATION AND THE ANALYTICAL MODEL, INCLUDING ICS EVENTS OCCURRING IN NEIGHBORING CRYSTALS, WITH (WITHOUT) ENERGY THRESHOLD AT 180 KEV

X-position [mm]	Simulation ( $\times 10^{-3}$ )	Model $\pm 0.002$ ( $\times 10^{-3}$ )
-15.125	$1.109 \pm 0.014$ ( $1.78 \pm 0.02$ )	1.143 (1.827)
-10.125	$1.249 \pm 0.018$ ( $2.006 \pm 0.018$ )	1.324 (2.100)
-5.125	$1.652 \pm 0.014$ ( $2.645 \pm 0.02$ )	1.731 (2.725)
0.125	$2.115 \pm 0.011$ ( $3.38 \pm 0.03$ )	2.219 (3.502)
5.125	$1.653 \pm 0.013$ ( $2.64 \pm 0.02$ )	1.733 (2.730)
10.125	$1.249 \pm 0.005$ ( $2.006 \pm 0.009$ )	1.337 (2.108)
15.125	$1.077 \pm 0.014$ ( $1.727 \pm 0.012$ )	1.146 (1.837)

TABLE II  
ICS SENSITIVITY IMAGE VALUES AT SEVEN DIFFERENT POSITIONS OVER THE CENTRAL X-AXIS, FOR THE SIMULATION AND THE ANALYTICAL MODEL, EXCLUDING ICS EVENTS OCCURRING IN NEIGHBORING CRYSTALS, WITH (WITHOUT) ENERGY THRESHOLD AT 180 KEV

X-position [mm]	Simulation ( $\times 10^{-3}$ )	Model $\pm 0.002$ ( $\times 10^{-3}$ )
-15.125	$0.575 \pm 0.007$ ( $0.904 \pm 0.014$ )	0.576 (0.920)
-10.125	$0.639 \pm 0.007$ ( $1.011 \pm 0.007$ )	0.676 (1.059)
-5.125	$0.865 \pm 0.009$ ( $1.349 \pm 0.013$ )	0.878 (1.364)
0.125	$1.084 \pm 0.010$ ( $1.70 \pm 0.02$ )	1.116 (1.730)
5.125	$0.877 \pm 0.008$ ( $1.352 \pm 0.017$ )	0.877 (1.364)
10.125	$0.642 \pm 0.006$ ( $1.010 \pm 0.012$ )	0.678 (1.058)
15.125	$0.549 \pm 0.009$ ( $0.873 \pm 0.010$ )	0.575 (0.924)

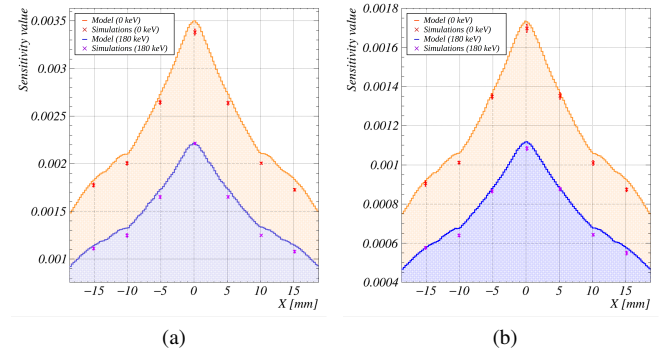


Fig. 4. Validation of the ICS analytical sensitivity image model with no energy threshold over the ICS events (orange line) and with a threshold of 180 keV (blue line) against Monte Carlo simulations (red and violet crosses, respectively). (a) including ICS occurring in neighboring crystals, and (b) discarding them. Each simulated  $X$ -position represents the mean of five independent simulations; the displayed error bars correspond to the standard error of the mean.

As expected, higher sensitivity values are obtained when including neighboring-crystal ICS events; indeed, when doing so, the sensitivity values almost increase twofold, independently of the energy threshold.

These results, which are also graphically displayed in figure 4, show a good agreement between the model predictions and the simulated data, although they also suggest that the ICS model slightly overestimates the probability of ICS detection when compared to the MC simulations (see Discussion). When including the neighboring-crystal ICS events (figure 4a), a mean discrepancy of 5.0 % (maximum: 6.6 %) is found with the energy cut at 180 keV; slightly lower discrepancy values are found without energy cuts (mean 4.0 %, maximum 5.9 %). The discrepancy is even lower when excluding the neighboring-crystal ICS events (figure 4b), with a mean value of 2.8 % (maximum: 5.4 %) found with the energy cut at 180 keV; very similar discrepancy values are found without energy cuts (mean 2.9 %, maximum 5.5 %).

Figure 5 shows some results regarding the 1 MBq MC-simulated cylinder source, which yielded 29 205 golden events

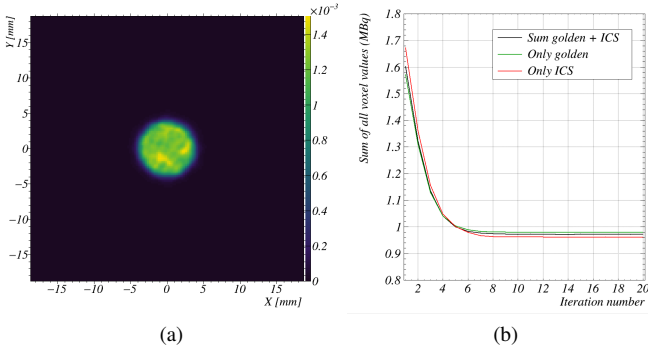


Fig. 5. Results with the 1 MBq MC-simulated cylinder source: (a) Transversal ( $XY$ ) projection at iteration 10 for golden and ICS events, with the color scale representing the activity in MBq recovered in the sum of voxels involved in the projection; (b) evolution of the total activity recovered in the golden and ICS, only golden and only ICS images by summing all the voxel values in the three cases.

and 16 058 ICS events (i.e. 65 % and 35 % of total, respectively). In particular, figure 5a shows the  $XY$ -projection at iteration 10 when using both ICS and golden events through the joint algorithm (14). Figure 5b shows the evolution of the sum of all voxel values against the LM-MLEM iteration number in the images obtained with the joint algorithm, and also when reconstructing independently with golden events and with ICS events. As the proposed model is quantitative, the sum of intensity values represents the reconstructed activity of the simulated source (in MBq); the ground truth value was 1 MBq in this case. While very close to this reference value, figure 5b shows that the algorithm converges to a slightly smaller value for all three sets of data (e.g. 0.96 MBq at iteration 20 using only ICS events). This observation is consistent with the aforementioned small overestimation of the model sensitivity image when compared with MC-simulations.

### C. IQ phantom simulation results

The IQ phantom simulation yielded a total of 125 541 golden events and 68 172 ICS events (i.e. 65 % and 35 % of total, respectively). Figure 6 shows the  $XY$ -projections over the uniform region of the IQ phantom at three different iterations (5, 10 and 20) and for different sets of MC-simulated data: only ICS events (bottom row), only golden events (central row) and both ICS and golden reconstructed through the joint algorithm (14). Figure 7 shows the  $XY$ -projections over the rods region of the phantom, for the same aforementioned iterations and sets of data. Visual inspection of the images reveals, as expected, an increased degradation at higher iterations of the iterative algorithm; but, importantly, it also reveals that the joint usage of ICS and golden events improves the uniformity in the corresponding phantom region, especially at higher iterations. The only-ICS images, even if they are not conceived for use, prove that these events contain valuable information about the activity distribution. Conversely, there is no appreciable degradation of the rods region when using ICS and golden events together, despite the use of V-LORs. Figure 8 provides quantitative grounds for these observations with the IQ metrics computed in the

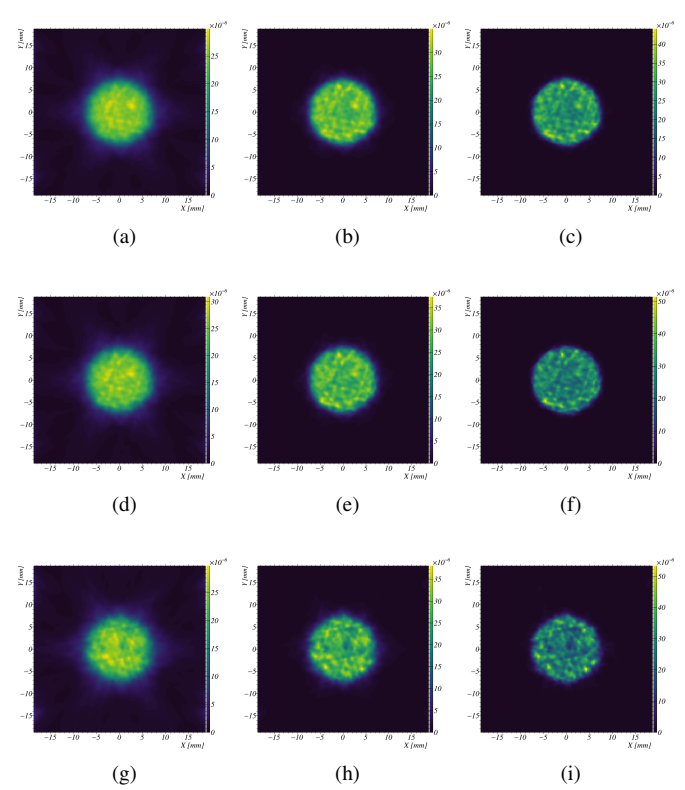


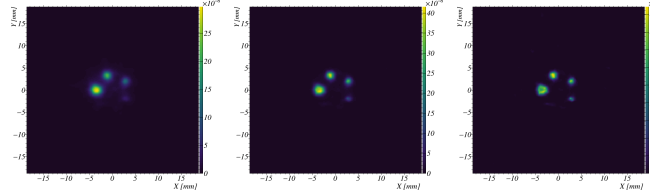
Fig. 6. Transversal ( $XY$ ) projections over the IQ-phantom uniformity region at iteration 5 (first column), 10 (second column) and 20 (third column) for golden and ICS (first row), only golden (second row) and only ICS (third row) events, obtained with simulations. The scale represents the activity in MBq recovered in the sum of voxels involved in each projection (e.g. a Z-row of voxels for the transversal projection).

uniform and rods regions, following the procedure described in section II.

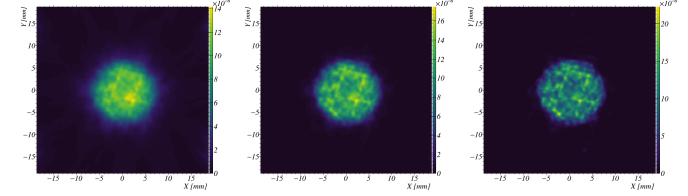
### D. IQ phantom experimental results

The IQ phantom experimental measurement with MERMAID yielded a total of 46 413 golden events and 21 368 ICS events (i.e. 68 % and 32 % of total, respectively). Figure 9 shows the  $XY$ -projections over the uniform region of the IQ phantom at three different iterations (5, 10 and 20) and for different sets of experimental data acquired with MERMAID: only ICS events (bottom row), only golden events (central row) and both ICS and golden reconstructed through the joint algorithm (14). The  $XY$ -projections over the rods region of the phantom are shown in Figure 10, for the same aforementioned number of iterations and data sets.

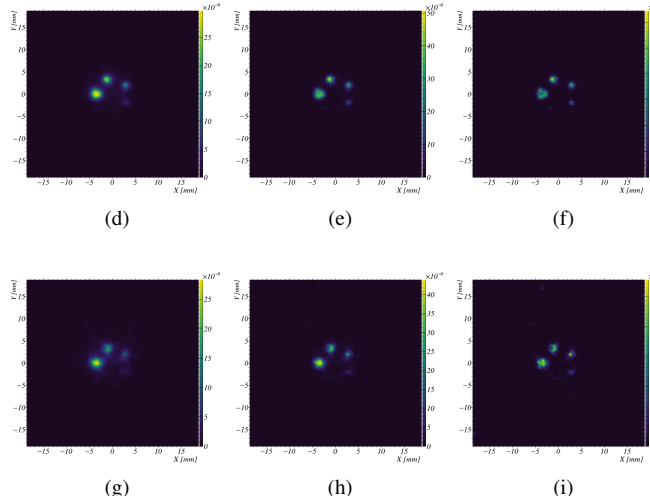
As expected, the overall image quality of the reconstructed experimental data is inferior to that of the MC simulated data, which can be attributed to data-degradation factors not present in the simulation, such as non-uniform SiPM response, limited energy resolution, etc. Nevertheless, similar observations as the ones made with MC simulations can be made; the joint usage of ICS and golden events improves the uniformity of the images when compared to only golden event images. Figure 11 shows the corresponding IQ metrics computed in the uniform and rods regions.



(a) (b) (c) (d) (e) (f) (g) (h) (i)

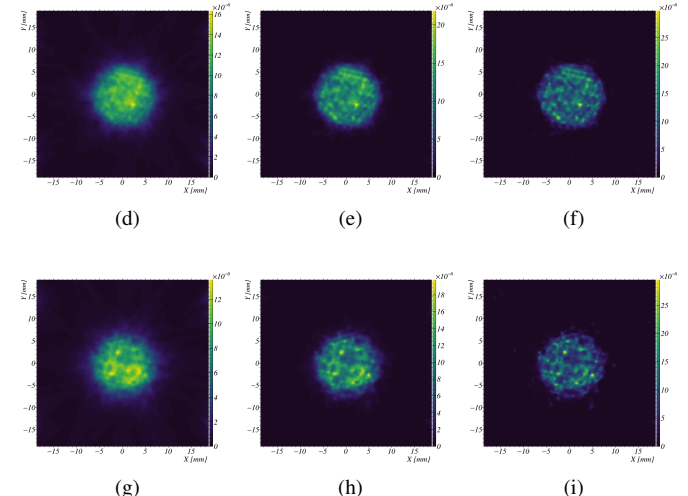


(a) (b) (c) (d) (e) (f) (g) (h) (i)



(a) (b) (c) (d) (e) (f) (g) (h) (i)

Fig. 7. Transversal (XY) projections over the NEMA rods region at iteration 5 (first column), 10 (second column) and 20 (third column) for golden and ICS (first row), only golden (second row) and only ICS (third row) events, obtained with MC simulations. The scale represents the activity in MBq recovered in the sum of voxels involved in each projection (e.g. a Z-row of voxels for the transversal projection).



(a) (b) (c) (d) (e) (f) (g) (h) (i)

Fig. 9. Transversal (XY) projections over the NEMA uniformity region at iteration 5 (first column), 10 (second column) and 20 (third column) for golden and ICS (first row), only golden (second row) and only ICS (third row) events, obtained with MERMAID. The scale represents the activity in MBq recovered in the sum of voxels involved in each projection (e.g. a Z-row of voxels for the transversal projection).

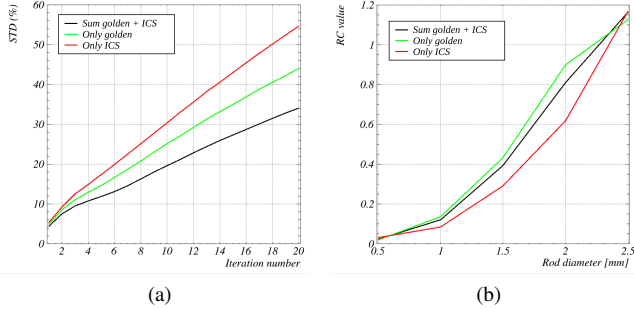


Fig. 8. IQ metrics obtained with MC simulated data. (a) Evolution of the percentage of standard deviation in the uniformity ROI in a range of LM-MLEM iterations. (b) Recovery coefficients for the five ROIs in the rods region at iteration 5.

#### IV. DISCUSSION

This work proposes a physics-based model of ICS events formation which leads to analytical expressions for the ICS sensitivity image and the system matrix needed for iterative reconstruction. The approach's main feature is that ICS events are not *selected* according to an algorithm that looks for the correct Compton scattering site or the *correct* LOR. ICS event-selection approaches are common in the literature, and their accuracy typically depends on the assumed PET geometry and readout, as well as the nature of the event-selection method.

It follows that, in a number of ICS events, the Compton scattering site is incorrectly determined and the event contributes to degrade the image, introducing noise and worsening the spatial resolution; the identification accuracy of these algorithms determines the degree of degradation. By contrast, the approach proposed here models all ICS events as V-LORs, which can be regarded as a more appropriate way to describe the information about the spatial emission distribution encoded in these events. The necessary trade-off resides in the fact that V-LORs are less informative than LORs; clearly, an ICS event-selection approach with accuracy equal or close to 100 % would perform better than the approach proposed in this work. It must be noted, however, that the addition of ICS events as regular LORs via an ICS event-selection approach should entail, in theory, a corresponding change in the sensitivity image which would then depend on the accuracy value of the approach; otherwise, the quantitative accuracy of the obtained images could be compromised. Another point to consider is that the proposed V-LORs approach does not require previous training based on large datasets or significant computational resources, as most machine-learning based approaches do.

Evidently, the construction of V-LORs requires the ability of the PET scanner to discriminate hits occurring in different PET detectors. As such, the proposed approach is particularly well-suited for PET concepts with one-to-one crystal-to-photosensor coupling, as they can provide information about

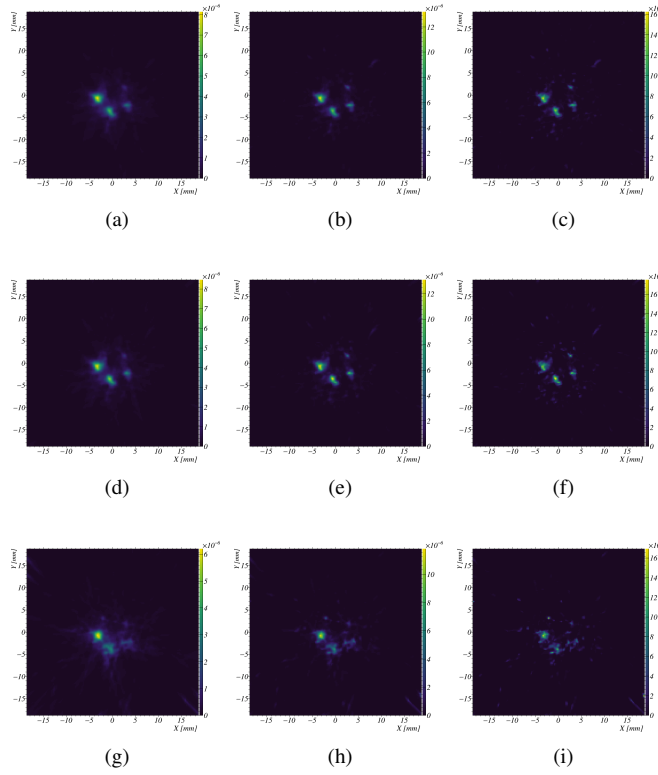


Fig. 10. Transversal (XY) projections over the NEMA rods region at iteration 5 (first column), 10 (second column) and 20 (third column) for golden and ICS (first row), only golden (second row) and only ICS (third row) events, obtained with MERMAID. The scale represents the activity in MBq recovered in the sum of voxels involved in each projection (e.g. a Z-row of voxels for the transversal projection).

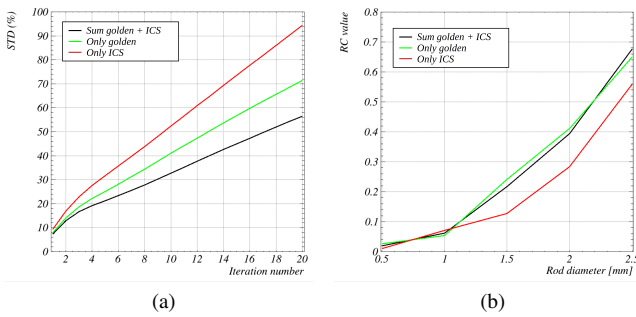


Fig. 11. Image quality metrics obtained with experimental data. (a) Evolution of the percentage of standard deviation in the uniformity ROI in a range of LM-MLEM iterations (b) Recovery coefficients for the five ROIs in the rods region at iteration 5.

the multiple interactions within the same module [35], [29], [36]. In the case of pixelated detector modules with shared readout or multiplexing architectures, the proposed model can be directly applied to inter-module ICS events. Furthermore, the blurring effects of ICS within the same module or within a monolithic crystal could be incorporated into the model also proposed here to handle conventional coincidence events (see Appendix B).

The proposed analytical models, when used in a statistical iterative algorithm such as LM-MLEM with ICS data, lead

to accurate quantification of the total reconstructed activity. This feature stands out from most existing techniques proposed to calculate system matrix and sensitivity image elements. Moreover, the work shows how such V-LOR-modeled ICS events can be used together with LOR-modeled golden events in a joint algorithm, increasing the sensitivity of the PET scanner while maintaining the quantitative accuracy of the total reconstructed activity in the images (see figure 5b). To this end, analytical expressions for the golden sensitivity image and the system matrix are also proposed (see Appendix B), essentially based on the ICS model without the scattered photon probability terms. The aforementioned quantitative accuracy of the total reconstructed activity is ensured under ideal detection conditions, i.e., assuming that the sets of data are composed of those (and only those) events that the models are based upon. Obviously, experimental data do not fulfill these ideal conditions; indeed, images obtained with experimental data exhibit lower quality than their MC-simulation counterparts. The rationale for this result can be attributed to several factors. First, the experimental measurements were acquired using a system that is still under development (e.g., a correction for non-uniform SiPM channel efficiencies has not yet been developed). In addition, a possible misalignment between the phantom and the scanner axes may have introduced some blurring when projecting all axial slices into a single image or inaccuracies when applying 3D ROIs; some defects in the 3D printing procedure might have also affected the empty cavities. Furthermore, the limited energy resolution of the system, together with potential light crosstalk effects, may have further degraded the performance of the approach as well as reducing the number of events detected.

Other experimental data-degradation effects which affect the performance of the reconstruction are random coincidences (both for golden and ICS), and object-scattered events. A particular example, which could be accounted for by enlarging the models correspondingly, is represented by those events detected as golden, but actually being ICS events in which the Compton scattering interaction remains undetected because of the energy windows and the limited energy resolution. More generally, conventional estimation techniques for random and object scatter might fail when broadening the energy window to capture ICS events, as shown for randoms in [37]. The implementation of strategies to compensate for such effects are out of the scope of this work, but will be required to allow for accurate quantification of experimental PET data.

The validation of the models, carried out by comparing the predictions of the ICS sensitivity image model with MC simulations of one-voxel sources, suggests that the former slightly overestimate the probability of ICS detection extracted from MC simulations. This observation is supported by the results with the MC-simulated cylinder source (figure 5b), in which the sum of all voxel values in the images yields values slightly smaller than the ground truth simulated activity. The reason for the discrepancy (of approximately 3 – 5 % in the ICS sensitivity image) can be traced back to the attenuation coefficient values used to estimate the sensitivity image and the system matrix, here extracted from the NIST database using linear interpolation; these values are not exactly the same em-

ployed by the MC simulation, as shown in Appendix B. In any case, the proposed models fulfill their purpose, which is not to provide values of the sensitivity image and the system matrix identical to those of a particular MC simulation platform, but rather to provide a reasonable compromise between accuracy and flexibility to efficiently adapt to any PET geometry.

Results clearly indicate that the joint usage of ICS and golden events improves the uniformity of homogeneous regions compared to the individual usage of golden events. This difference is observed both with MC simulations of the IQ phantom (figure 8a) and with experimental data (figure 11a), and becomes more pronounced at higher iterations of the iterative algorithm. In contrast, the recovery coefficients slightly decrease when including ICS events modeled as V-LORs; again, this result is observed both with MC simulations of the IQ phantom (figure 8b) and with experimental data (figure 11b). Recovery coefficients are associated to the spatial resolution of the system and, although its characterization via the low-activity, downscaled IQ phantom is suboptimal (including the procedure followed to obtain the recovery coefficients, as mentioned in section II), degradation in the image spatial resolution can be a consequence of combining two channels of information: the highly informative channel corresponding to the golden events (modeled as LORs), and a less informative channel (the ICS events modeled as V-LORs). Indeed, this effect is also observed in other usages of joint algorithms, e.g., with the different two- and three-interaction channels of a Compton camera [25], and also plays a role in the SOR metric, see Appendix C. However, the slight loss of resolution is not visually appreciable in the reconstructed images, while there is an observable reduction in background noise. The noise reduction could be even more significant for PET configurations suffering from very high ICS fractions, such as those with dual or triple detector layers.

Finally, it must be noted that the formulation of the proposed model leaves the door open for a number of potential improvements. First, it is not restricted to voxels, and could be extended to other discretization schemes such as blobs [38]. Second, acolinearity effects can be modeled by replacing the Dirac delta  $\delta(\Omega_0 + \Omega'_0)$  in (4) by a suitable term accounting for this effect, at the cost of increasing the complexity of the model and its computation. Third, different attenuation values of detector and non-detector materials, including object attenuation, can be readily included in the model via suitable exponential survival terms. Lastly, the current formulation of the model does not make use of the detected deposited energy in the two singles where the ICS-photon is involved; instead, synthetic deposited energies are estimated via the Compton equation and used in the estimation of the attenuation coefficients of the models. This redundant information between the Compton-equation derived deposited energies and the actually measured ones can be exploited by incorporating a measurement noise distribution function to the model [39], [40], or through the weights  $w_1$  and  $w_2$  in (12). The implementation and evaluation of potential improvements to the ICS model, together with its comparison with event-selection methods available in the literature, is foreseen in a future study.

## V. CONCLUSION

In this work, a physics-based model of ICS in PET is proposed and validated. The model is shown to yield reasonably accurate analytical expressions of the sensitivity image and the system matrix, where ICS events are modeled as V-LORs without the need to identify the Compton scattering site. The work shows that such V-LOR-modeled ICS events, when included to conventional events in a joint algorithm, allow improving the uniformity in an IQ phantom, at the cost of slightly decreasing the recovery coefficients; such results are obtained both with MC-simulations and with experimental data acquired with MERMAID, the latter for a phantom with activity well below that of conventional small-animal scenarios. The proposed approach, which can be easily adapted to any PET geometry, could be particularly beneficial in low-count PET scenarios, where the detection sensitivity is a limiting factor.

## APPENDIX A NOMENCLATURE

Table III summarizes the main symbols employed in this work and their definitions.

TABLE III  
NOMENCLATURE

Symbol	Description
$\vec{r}_0$	Annihilation photon emission position
$\Omega_0, \Omega'_0$	Annihilation photon emission directions
$\vec{r}_1$	Photoabsorption position undergone by the non-ICS photon
$\vec{r}_2, \vec{r}_3$	Interaction positions undergone by the ICS photon
$D_i$	PET detector where photon interaction given by $\vec{r}_i$ occurs
$\ell_1$	Length in the $\vec{r}_1 - \vec{r}_0$ direction
$\Delta\ell_1$	Amount of $\ell_1$ in detector material
$\ell_2$	Length in the $\vec{r}_1 - \vec{r}_0$ direction
$\Delta\ell_2$	Amount of $\ell_2$ in detector material
$\ell_3$	Length in the $\vec{r}_3 - \vec{r}_2$ direction
$\Delta\ell_3$	Amount of $\ell_3$ in detector material
$\ell'_3, \ell'_1$	Length in the $\vec{r}_3 - \vec{r}_1$ direction
$\xi$	Length in the $\vec{r}_2 - \vec{r}_1$ direction
$\Delta\ell'_3 + \Delta\ell'_1$	Amount of $\ell'_3, \ell'_1$ in detector material
$\mu_i$	Total attenuation in detector after $\vec{r}_i$
$\mu_i^e$	Photoelectric attenuation in detector after interaction in $\vec{r}_i$
$d\sigma_0^C/d\Omega_i$	Differential Klein-Nishina cross section
$n_e$	Effective number density of electrons in the detector

## APPENDIX B ANALYTICAL MODEL FOR CONVENTIONAL COINCIDENCES (GOLDEN EVENTS)

The differential probability for an emission to be detected through two energy depositions within the photopeak (or, in other words, to become a golden event) can be expressed as

$$dP^G = \frac{d^3 r_0}{V} \Theta_v(\vec{r}_0) \frac{d\Omega_0}{4\pi} \frac{d\Omega'_0}{4\pi} 4\pi \delta(\Omega_0 + \Omega'_0) e^{-\mu_0 \Delta\ell_1} \mu_0^e d\ell_1 \cdot e^{-\mu_0 \Delta\ell_2} \mu_0^e d\ell_2, \quad (15)$$

where the absence of the leading factor 2 should be noted. Next, the change of variables  $\{\vec{r}_0, \Omega_0, \ell_1, \ell_2\} \rightarrow \{\vec{r}_1, \vec{r}_2, \xi\}$  allows obtaining the following expression for the sensitivity image element:

$$s_v^G = \frac{1}{4\pi V} \int_{\vec{r}_1 \in PET} d^3 r_1 \int_{\vec{r}_2 \in PET} d^3 r_2 \int_{\xi \in \mathbb{R}^+} d\xi \Theta_v(\xi) \cdot \frac{e^{-\mu_0(\Delta\ell_1 + \Delta\ell_2)} (\mu_0^e)^2}{|\vec{r}_1 - \vec{r}_2|^2}, \quad (16)$$

and the following probability density:

$$\frac{dP^G}{d^3 r_1 d^3 r_2} = \frac{1}{4\pi V} \int_{\xi \in \mathbb{R}^+} d\xi \Theta_v(\xi) \frac{e^{-\mu_0(\Delta\ell_1 + \Delta\ell_2)} (\mu_0^e)^2}{|\vec{r}_1 - \vec{r}_2|^2}, \quad (17)$$

from which the system matrix elements  $H_{iv}^G$  can be derived:

$$h_{iv}^G = \int_{\vec{r}_1, \vec{r}_2 \in \Delta\eta_i} d^3 r_1 d^3 r_2 \frac{dP^G}{d^3 r_1 d^3 r_2} \quad (18)$$

The mathematical expression for the sensitivity image (16) was validated against Monte Carlo simulations in a manner equivalent to the ICS counterpart. Figure 12 shows the results of such validation. In addition, the figure shows the resulting model sensitivity image when the total and photoelectric attenuation coefficients at 511 keV,  $\mu_0$  and  $\mu_0^e$ , are estimated directly from a dedicated MC simulation, instead of using the NIST database. The simulation to obtain an estimate of the attenuation coefficients consisted of a 511 keV collimated photon source impinging on a single LYSO elongated detector; in this way, the distribution of the first photon interaction (if any) within the detector follows the distribution  $e^{-\mu_0 \Delta x} \cdot \mu_0^e$ . The fit yielded the values  $\mu_0^e = 0.02646 \pm 0.00010 \text{ mm}^{-1}$ ,  $\mu_0 = 0.0857 \pm 0.0003 \text{ mm}^{-1}$ , resulting in the green-line distribution of figure 12. These numbers are to be compared with the NIST-interpolated values of  $\mu_0^e = 0.0266467 \pm 0.000007 \text{ mm}^{-1}$ ,  $\mu_0 = 0.08527 \pm 0.000007 \text{ mm}^{-1}$  resulting in the blue-line distribution shown also in figure 12.

Note that these results apply to the attenuation coefficients for photons with 511 keV energy, which are employed in the analytical models for golden events; the small discrepancy found between the NIST and simulation-derived attenuation coefficient might not necessarily be the same at different photon energies.

## APPENDIX C

### IQ-PHANTOM INSERT REGION RESULTS

Figure 13 shows the  $XY$ -projections over the inserts region of the IQ phantom at three different iterations (5, 10 and 20) and for different sets of MC-simulated data: only ICS events (bottom row), only golden events (central row) and both ICS and golden reconstructed through the joint algorithm (14). Figure 14 shows the corresponding information for experimental data. Finally, figure 15 shows the evolution of the SOR computed following the NEMA protocol adapted to the downscaled size of the phantom, for one of the two air inserts with both simulated and experimental data.

As with the rods and uniform regions of the IQ phantom, the images obtained with experimental data exhibit higher degradation when compared with the simulated data ones. Similar

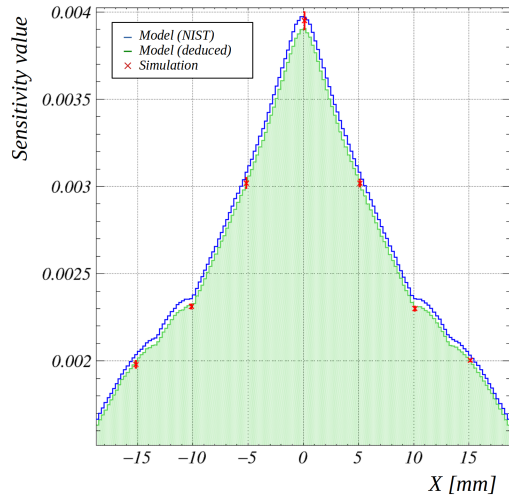


Fig. 12. Validation of the golden analytical sensitivity image model with the attenuation coefficient extracted from the NIST database (blue line) and deduced from simulations (green line), against Monte Carlo simulations (red crosses). Each simulated  $X$ -position represents the mean of five independent simulations; the displayed error bars correspond to the standard error of the mean.

to the results with the RCs, the SOR values are slightly better when using only golden events as compared to the situation where ICS events are included. Again, this outcome can be regarded as a logical consequence of combining the highly informative channel of golden events (modeled as LORs), and a less informative channel (the ICS events modeled as V-LORs); in particular, the section of the V-LOR not containing the emission point might cross the inserts, thus placing activity there. In any case, this difference is only noticeable quantitatively in the experimental case; as such, the influence of further degradation effects (optical sharing, randoms, object scatter) over the different channels of information (golden and ICS events) remains to be investigated.

## ACKNOWLEDGMENT

This work was supported by the Alexander von Humboldt foundation and the German Research Foundation (DFG) under grant agreement no. 496099829.

## REFERENCES

- [1] E. Enlow and S. Abbaszadeh, "State-of-the-art challenges and emerging technologies in radiation detection for nuclear medicine imaging: A review," *Frontiers in Physics*, vol. Volume 11 - 2023, 2023.
- [2] C. Mingels *et al.*, "Dose Reduction in Pediatric Oncology Patients with Delayed Total-Body [18F]FDG PET/CT," *Journal of Nuclear Medicine*, vol. 65, no. 7, pp. 1101–1106, 2024.
- [3] C. S. Burton *et al.*, "Fetal Dose from PET and CT in Pregnant Patients," *Journal of Nuclear Medicine*, vol. 64, no. 2, pp. 312–319, 2023.
- [4] T. Carlier, K. P. Willowson, E. Fourkal, D. L. Bailey, M. Doss, and M. Conti, "90Y -PET imaging: Exploring limitations and accuracy under conditions of low counts and high random fraction," *Medical Physics*, vol. 42, no. 7, pp. 4295–4309, 2015.
- [5] I. Ozoemelam *et al.*, "Real-Time PET Imaging for Range Verification of Helium Radiotherapy," *Frontiers in Physics*, vol. Volume 8 - 2020, 2020.

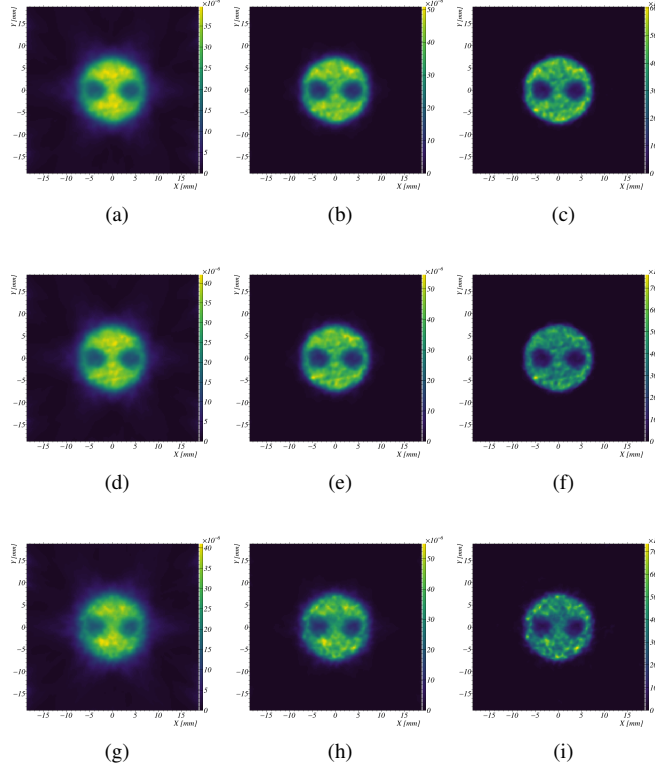


Fig. 13. Transversal (XY) projections over the NEMA inserts region at iteration 5 (first column), 10 (second column) and 20 (third column) for golden and ICS (first row), only golden (second row) and only ICS (third row) events, obtained with MC-simulated data. The scale represents the activity in MBq recovered in the sum of voxels involved in each projection (e.g. a Z-row of voxels for the transversal projection).

- [6] M. Zvolský, M. Schaar, S. Seeger, S. Rakers, and M. Rafecas, “Development of a digital zebrafish phantom and its application to dedicated small-fish PET,” *Physics in Medicine and Biology*, vol. 67, no. 17, p. 175005, aug 2022. [Online]. Available: <https://doi.org/10.1088/1361-6560/ac71ee>
- [7] F. Godinez, C. Mingels, R. Bayerlein, B. Mehadji, and L. Nardo, “Total Body PET/CT: Future Aspects,” *Seminars in Nuclear Medicine*, vol. 55, no. 1, pp. 107–115, 2025, total body PET/CT.
- [8] A. Sanaat, M. Amini, H. Arabi, and H. Zaidi, “The quest for multifunctional and dedicated PET instrumentation with irregular geometries,” *Annals of Nuclear Medicine*, vol. 38, no. 1, pp. 31–70, 2024.
- [9] H. Phuc Vo, T. Williams, K. Doroud, C. Williams, and M. Rafecas, “Dedicated prostate DOI-TOF-PET based on the ProVision detection concept,” *Physics in Medicine and Biology*, vol. 70, no. 18, p. 185001, sep 2025.
- [10] A. Sanaat, H. Arabi, M. Reza Ay, and H. Zaidi, “Novel preclinical PET geometrical concept using a monolithic scintillator crystal offering concurrent enhancement in spatial resolution and detection sensitivity: a simulation study,” *Physics in Medicine and Biology*, vol. 65, no. 4, p. 045013, 2020.
- [11] Z. Kuang *et al.*, “Physical and imaging performance of SIAT aPET under different energy windows and timing windows,” *Medical Physics*, vol. 49, no. 3, pp. 1432–1444, 2022.
- [12] E. Petersen, A. LaBella, Y. Li, Z. Wang, and A. H. Goldan, “Resolving inter-crystal scatter in a light-sharing depth-encoding PET detector” *Physics in Medicine and Biology*, vol. 69, no. 3, p. 035024, feb 2024.
- [13] H. Zou *et al.*, “Impact of inter-crystal scattering on image quality of a dedicated brain PET scanner with DOI capability,” *Physics in Medicine and Biology*, vol. 70, no. 23, p. 235003, 2025.
- [14] M. Rafecas, G. Böning, B. J. Pichler, E. Lorenz, M. Schwaiger, and S. I. Ziegler, “Inter-crystal scatter in a dual layer, high resolution LSO-APD positron emission tomograph,” *Physics in Medicine and Biology*, vol. 48, no. 7, p. 821, mar 2003.
- [15] M. S. Lee, H. S. Shim, and J. S. Lee, “Strategies for mitigating inter-

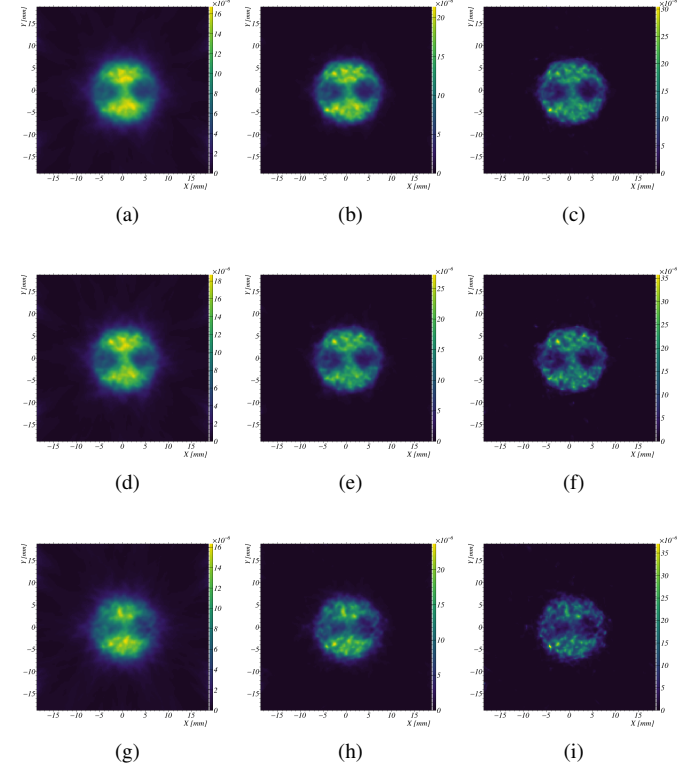


Fig. 14. Transversal (XY) projections over the NEMA inserts region at iteration 5 (first column), 10 (second column) and 20 (third column) for golden and ICS (first row), only golden (second row) and only ICS (third row) events, obtained with MERMAID. The scale represents the activity in MBq recovered in the sum of voxels involved in each projection (e.g. a Z-row of voxels for the transversal projection).

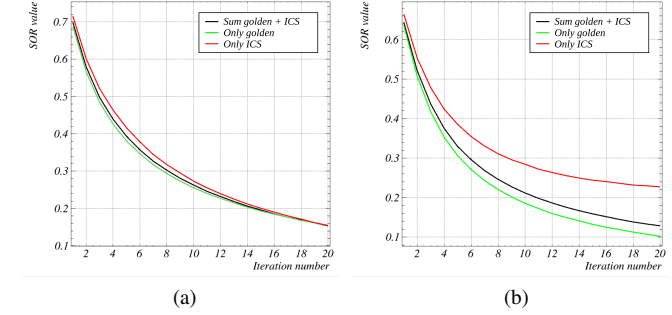


Fig. 15. SOR metrics obtained in one of the IQ-phantom inserts with (a) MC-simulated data; (b) experimental data.

- crystal scattering effects in positron emission tomography: a comprehensive review,” *Biomedical Engineering Letters*, vol. 14, no. 6, pp. 1243–1258, 2024.
- [16] K. Comanor, P. Virador, and W. Moses, “Algorithms to identify detector Compton scatter in PET modules,” *IEEE Transactions on Nuclear Science*, vol. 43, no. 4, pp. 2213–2218, 1996.
- [17] G. Pratx and C. S. Levin, “Bayesian reconstruction of photon interaction sequences for high-resolution pet detectors,” *Physics in Medicine and Biology*, vol. 54, no. 17, p. 5073, 2009.
- [18] E. Lage *et al.*, “Recovery and normalization of triple coincidences in PET,” *Medical Physics*, vol. 42, no. 3, pp. 1398–1410, 2015.
- [19] M. S. Lee, S. K. Kang, and J. S. Lee, “Novel inter-crystal scattering event identification method for PET detectors,” *Physics in Medicine and Biology*, vol. 63, no. 11, p. 115015, 2018.
- [20] J.-B. Michaud *et al.*, “Sensitivity Increase Through a Neural Network Method for LOR Recovery of ICS Triple Coincidences in High-

- Resolution Pixelated- Detectors PET Scanners,” *IEEE Transactions on Nuclear Science*, vol. 62, no. 1, pp. 82–94, 2015.
- [21] C. Wu, M. S. Lee, and C. S. Levin, “Neural Network-based Inter-crystal Scatter Event Positioning in a PET System Design Based on 3D Position Sensitive Detectors,” in *2020 IEEE Nuclear Science Symposium and Medical Imaging Conference (NSS/MIC)*, 2020, pp. 1–3.
- [22] S. Lee and J. S. Lee, “Inter-crystal scattering recovery of light-sharing PET detectors using convolutional neural networks,” *Physics in Medicine and Biology*, vol. 66, no. 18, p. 185004, sep 2021.
- [23] J. E. Gillam *et al.*, “Sensitivity recovery for the AX-PET prototype using inter-crystal scattering events,” *Physics in Medicine and Biology*, vol. 59, no. 15, p. 4065, 2014.
- [24] M. Grkovski *et al.*, “Evaluation of a high resolution silicon PET insert module,” *Nuclear Instruments and Methods in Physics Research Section A: Accelerators, Spectrometers, Detectors and Associated Equipment*, vol. 788, pp. 86–94, 2015.
- [25] J. Roser *et al.*, “Joint image reconstruction algorithm in compton cameras,” *Physics in Medicine and Biology*, vol. 67, no. 15, p. 155009, jul 2022.
- [26] ——, “Image reconstruction for a multi-layer Compton telescope: an analytical model for three interaction events,” *Physics in Medicine and Biology*, vol. 65, no. 14, p. 145005, jul 2020.
- [27] R. L. Siddon, “Prism representation: a 3D ray-tracing algorithm for radiotherapy applications,” *Physics in Medicine and Biology*, vol. 30, no. 8, p. 817, 1985.
- [28] A. H. Compton, “A Quantum Theory of the Scattering of X-rays by Light Elements,” *Phys. Rev.*, vol. 21, pp. 483–502, May 1923.
- [29] S. Seeger, H. P. Vo, A. Bolke, and M. Rafecas, “Characterisation of the Upgraded MERMAID Prototype, a PET/CT Device for Small Aquatic Animals,” in *2022 IEEE Nuclear Science Symposium and Medical Imaging Conference (NSS/MIC)*, 2022, pp. 1–2.
- [30] N. E. M. Association *et al.*, “Performance measurements of small animal positron emission tomographs,” *NEMA Standards Publication, NU4-2008*, pp. 1–23, 2008. [Online]. Available: <https://www.nema.org/docs/default-source/standards-document-library/nu-4-2008-website.pdf>
- [31] E. Elmoujarkach *et al.*, “Dedicated 3D-Printed Radioactive Phantoms With  $^{18}\text{F}$ -FDG for Ultrahigh-Resolution PET,” *IEEE Transactions on Radiation and Plasma Medical Sciences*, vol. 9, no. 3, pp. 362–371, 2025.
- [32] P. Hallen, D. Schug, and V. Schulz, “Comments on the NEMA NU 4-2008 standard on performance measurement of small animal positron emission tomographs,” *EJNMMI physics*, vol. 7, no. 1, p. 12, 2020.
- [33] S. Jan *et al.*, “GATE: a simulation toolkit for PET and SPECT,” *Physics in Medicine and Biology*, vol. 49, no. 19, p. 4543, 2004.
- [34] M. Berger *et al.*, “XCOM: Photon Cross Section Database (version 1.5),” 2010, NIST, PML, Radiation Physics Division (available online).
- [35] R. Ota, T. Omura, R. Yamada, T. Miwa, and M. Watanabe, “Evaluation of a Sub-Millimeter Resolution PET Detector With a 1.2 mm Pitch TSV-MPPC Array One-to-One Coupled to LFS Scintillator Crystals and Inter-Crystal Scatter Studies With Individual Signal Readout,” *IEEE Trans. Rad. Plasma. Med. Sci.*, vol. 1, no. 1, pp. 15–22, 2017.
- [36] N. Cucarella, J. Barrio, D. Sanchez, J. M. Benlloch, and A. J. Gonzalez, “Single-Ended Readout PET Detector Based on Pixelated Crystals With TOF and DOI Capabilities,” *TRPMS*, vol. 9, no. 7, pp. 866–871, 2025.
- [37] I. Torres-Espallardo, M. Rafecas, V. Spanoudaki, D. McElroy, and S. Ziegler, “Effect of inter-crystal scatter on estimation methods for random coincidences and subsequent correction,” *Physics in Medicine & Biology*, vol. 53, no. 9, p. 2391, 2008.
- [38] A. Lougovski, J. Hofheinz, J. Maus, G. Schramm, and J. van den Hoff, “On the relation between Kaiser–Bessel blob and tube of response based modelling of the system matrix in iterative PET image reconstruction,” *Physics in Medicine and Biology*, vol. 60, no. 10, p. 4209, 2015.
- [39] A. Sauve, A. Hero, W. Rogers, S. Wilderman, and N. Clinthorne, “3d image reconstruction for a compton spect camera model,” *IEEE Transactions on Nuclear Science*, vol. 46, no. 6, pp. 2075–2084, 1999.
- [40] Y. Du, Z. He, G. Knoll, D. Wehe, and W. Li, “Evaluation of a Compton scattering camera using 3-D position sensitive CdZnTe detectors,” *Nuclear Instruments and Methods in Physics Research Section A: Accelerators, Spectrometers, Detectors and Associated Equipment*, vol. 457, no. 1, pp. 203–211, 2001.